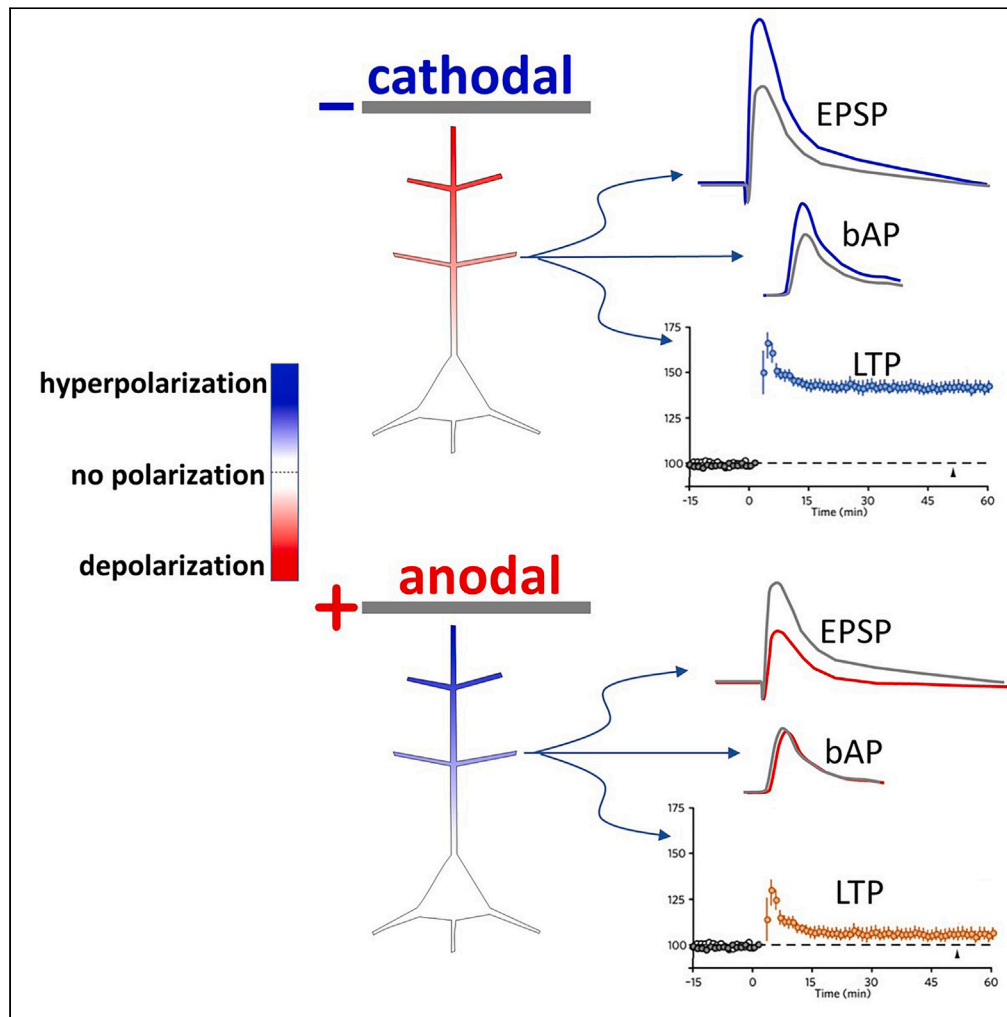# iScience

Article

Dendritic effects of tDCS insights from a morphologically realistic model neuron

Rahul Kumar Rathour, Hanoch Kaphzan

hkaphzan@univ.haifa.ac.il

Highlights

tDCS modulates the amplitude of the local dendritic excitatory postsynaptic potential

Only cathodal tDCS modulates the backpropagating action potential

Dendritic effects of tDCS are sufficient to modulate the input-output relationship

tDCS differentially modulates LTP at the distal region of the dendrite

Article

Dendritic effects of tDCS insights from a morphologically realistic model neuron

Rahul Kumar Rathour[1] and Hanoch Kaphzan[1,2,*]

SUMMARY

Transcranial direct current stimulation (tDCS) induces subcellular compartmental-dependent polarization, maximal in the distal portions of axons and dendrites. Using a morphologically realistic neuron model, we simulated tDCS-induced membrane polarization of the apical dendrite. Thus, we investigated the differential dendritic effects of anodal and cathodal tDCS on membrane potential polarization along the dendritic structure and its subsequent effects on dendritic membrane resistance, excitatory postsynaptic potential amplitude, backpropagating action potential amplitude, input/output relations, and long-term synaptic plasticity. We further showed that the effects of anodal and cathodal tDCS on the backpropagating action potential were asymmetric, and explained this asymmetry. Additionally, we showed that the effects on input/output relations were rather weak and limited to the low-mid range of stimulation frequencies, and that synaptic plasticity effects were mostly limited to the distal portion of the dendrite. Thus, we demonstrated how tDCS modifies dendritic physiology due to the dendrite's unique morphology and composition of voltage-gated ion channels.

INTRODUCTION

Transcranial direct current stimulation (tDCS) is a non-invasive brain stimulation therapeutic method that has gained increasing popularity. Multiple studies have shown the efficacy of tDCS in treating multiple neurological and psychiatric indications and have shown its ability to modulate cognitive functioning.[1] In principle, tDCS is performed by placing electrodes, anode and cathode, over the scalp and applying a weak direct current between these electrodes, thus delivering a subthreshold current across the brain tissue. This produces a few millivolts changes in membrane potential, well below the action potential threshold.[2] Early studies in humans showed that application of low intensity subthreshold direct current via the scalp was sufficient to induce measurable neurophysiological changes,[3] and that these effects are dependent on various ion channels.[4] Depending on the polarity of the electrical field (anodal vs. cathodal) and its orientation in relation to the neuronal axo-dendritic axis, it induces a relatively small (a few millivolts) incremental membrane polarization across the neuron, generating depolarization of one side and hyperpolarization of the other in a subcellular compartmental manner.[5–7]

Despite multiple studies of tDCS, its effects on neuronal cellular physiology have not been fully investigated. This lacuna is even more surprising when looked through the lens of dendritic physiology, as most studies of the cellular effects of tDCS have been on the axons. Assessing the effect of tDCS on dendritic physiology using experimental techniques (e.g., patch clamp) would be extremely difficult. That is why so far studies have investigated tDCS mostly using indirect transcranial measurements of local field potentials,[4,8] and only a few studies measured more invasive extracellular measurements such as local field potentials and voltage-sensitive imaging *ex vivo*[7] and *in vivo*,[9,10] but no direct recording from dendrites was ever performed in the context of tDCS. Dendrites are thin caliber structures, and performing electrophysiological recordings from these structures is very challenging, especially in the distal dendritic region, where tDCS' effects are maximal. Therefore, to assess the effects of tDCS on dendritic physiology, we utilized a morphologically and biophysically realistic conductance-based computational modeling approach.[11,12] First, we modeled cathodal/anodal stimulation by directly injecting depolarizing/hyperpolarizing current in the distal region of the dendrite. We assessed the effects of tDCS by measuring various physiologically relevant measurements before and during the simulated current injection.

Using this computational model, we show that cathodal stimulation increases dendritic input resistance whereas anodal stimulation decreases dendritic input resistance. We further show that cathodal stimulation increases local excitatory postsynaptic potential (EPSP) amplitude while anodal stimulation decreases local EPSP amplitude. Looking into backpropagating action potential dynamics, we found that cathodal stimulation increases backpropagating action potential amplitude in distal dendrites. Finally, using BCM-like synaptic plasticity rule, we show that cathodal stimulation increased long-term potentiation (LTP) magnitude whereas anodal stimulation decreased LTP magnitude.

In summary, using a modeling approach we demonstrate that tDCS induces significant modification of dendritic physiology, culminating with changes that can account for long-lasting plasticity modulations in functional neurons.

---

[1]Sagol Department of Neurobiology, University of Haifa, Haifa, Israel
[2]Lead contact
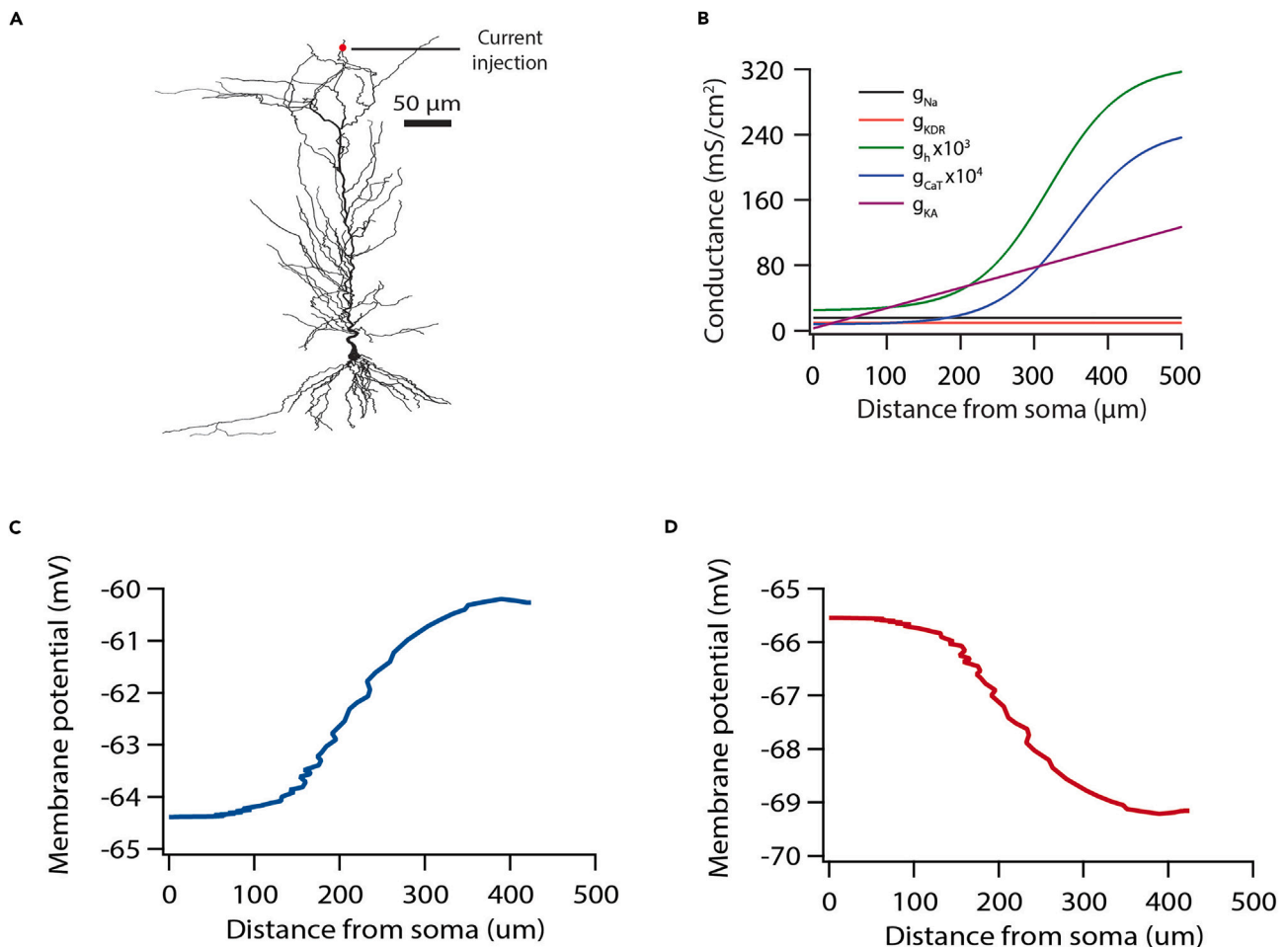*Correspondence: hkaphzan@univ.haifa.ac.il

Figure 1. Modeling of tDCS

To model tDCS-induced polarization of membrane potential, constant current was injected at distal end of apical dendrite of amplitude ± 200 pA (A) A 3D reconstructed neuronal morphology used as a substrate in this study.

(B) Types of voltage-gated ion channels and their distribution along the neuronal arbor, used in this study.

(C) Simulating cathodal tDCS by +200 pA constant current injection at the distal tip of the apical dendrite shows a decaying depolarization of the membrane potential along the apical dendrite toward the soma.

(D) Simulating anodal tDCS by −200 pA constant current injection at the distal tip of the apical dendrite shows a decaying hyperpolarization of membrane potential along the apical dendrite toward the soma.

RESULTS

Current injection at the apical dendrite tip induces similar membrane polarization to an extrinsically applied electric field

In order to test the effect of tDCS on dendritic physiology, we utilized a previously derived CA1 neuron model which was biophysically constrained, morphologically realistic, and expressing gradients of various voltage-gated ion channels (VGICs) (Figures 1A and 1B).[11–13] Specifically, our model neurons expressed five VGICs: fast Na^+, delayed rectifier K^+, A-type K^+, T-type Ca^{++}, and hyperpolarization-activated cyclic nucleotide–gated (HCN) channels. This model was hand-tuned in such a way that six coexistent functional maps matched their experimental counterparts.[11–13] Next, as mentioned earlier, we modeled tDCS-induced membrane potential polarization, by simulating a direct injection of constant current at the terminal end of the main apical dendrite. For cathodal stimulation +200 pA and for anodal stimulation −200 pA current was injected. Although naive, this type of tDCS simulation enabled to study the isolated dendritic effects of subthreshold membrane polarization. Moreover, it resembled the effects of tDCS, as this tDCS modeling ensured that membrane potential from the soma toward the dendritic tip did not change up to 150 μm from the soma, and from there on it steeply changed and saturated toward the site of the current injection (Figures 1C and 1D). Moreover, from examining the voltage decay along the dendritic trunk, we measured the length constant of the dendritic trunk to be 211 μm for cathodal tDCS and 232 μm for anodal tDCS. This modeling of tDCS was inspired by previous reports on modeling the polarization of neurons by extrinsically applied electric fields.[5]
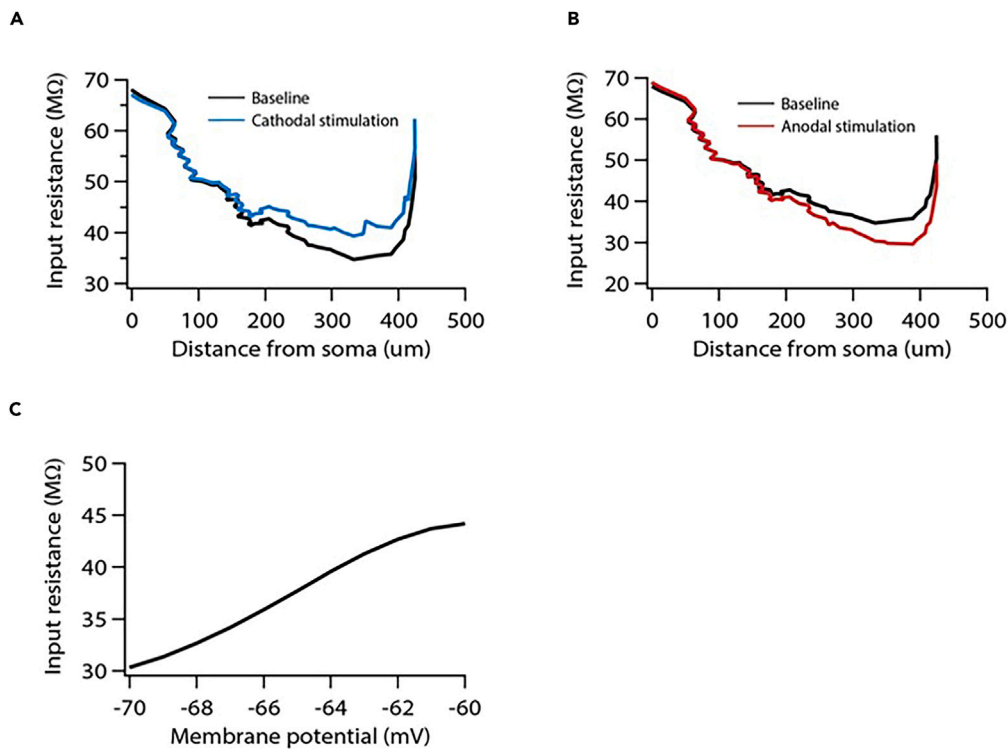
Figure 2. tDCS modifies input resistance along the dendrite
(A) Cathodal stimulation increases input resistance at distal dendrite.
(B) Anodal stimulation decreases input resistance at distal dendrite.
(C) Dependence of input resistance on membrane potential.

Simulation shows tDCS-induced alteration of the dendritic input resistance

Once the parameters of the model were established, we assessed the impact of tDCS on dendritic input resistance. As expected, input resistance is affected mainly at the distal end of the dendrite (Figures 2A and 2B), and this effect decays with distance toward the soma. Specifically, cathodal stimulation tends to increase input resistance, whereas anodal stimulation decreases input resistance at distal dendrite. These effects gradually faded along the dendrite toward the soma.

In order to understand the mechanistic basis for the observed effects of tDCS on input resistance, we first looked into the relationship between input resistance and membrane potential polarization (Figure 2C). For this, we chose the input resistance recording location along the apical dendrite where the effect of tDCS on input resistance was maximal. By doing so we found that the input resistance increased at depolarized potentials whereas membrane potential hyperpolarization reduced the input resistance (Figure 2C). These findings coincide with experimental observations in CA1 neuronal dendrite, which explained the effects of membrane polarization on input resistance via the modulation of the I_h current that is via the HCN channels,[14,15] and can further clarify the observed results of how tDCS affects input resistance. Given that cathodal stimulation induces membrane potential depolarization (Figure 1C), in turn, it deactivates HCN channels subsequently increasing input resistance (Figure 2A). On the other hand, anodal stimulation induces membrane potential hyperpolarization (Figure 1D), which subsequently activates more HCN channels, thus reducing input resistance (Figure 2B).

tDCS modifies the EPSP amplitude

Next, we aimed to investigate the active properties of the dendrite. First, we assessed the impact of tDCS on local EPSP amplitude (Figure 3). In doing so, we found that cathodal stimulation increased local EPSP amplitude (Figure 3A) while anodal stimulation reduced local EPSP amplitude (Figure 3B). As expected, this effect of tDCS took place in the distal dendrite. The reason for the change in EPSP amplitude with tDCS is the alteration of the input resistance. As cathodal stimulation depolarizes membrane potential, the input resistance gets increased, subsequently increasing also the local EPSP amplitude. On the other hand, anodal stimulation hyperpolarizes membrane potential causing a decrease in input resistance, and hence local EPSP amplitude decreases. This should be noted that all other parameters which might affect EPSP amplitude were fixed across different conditions (baseline vs. tDCS).
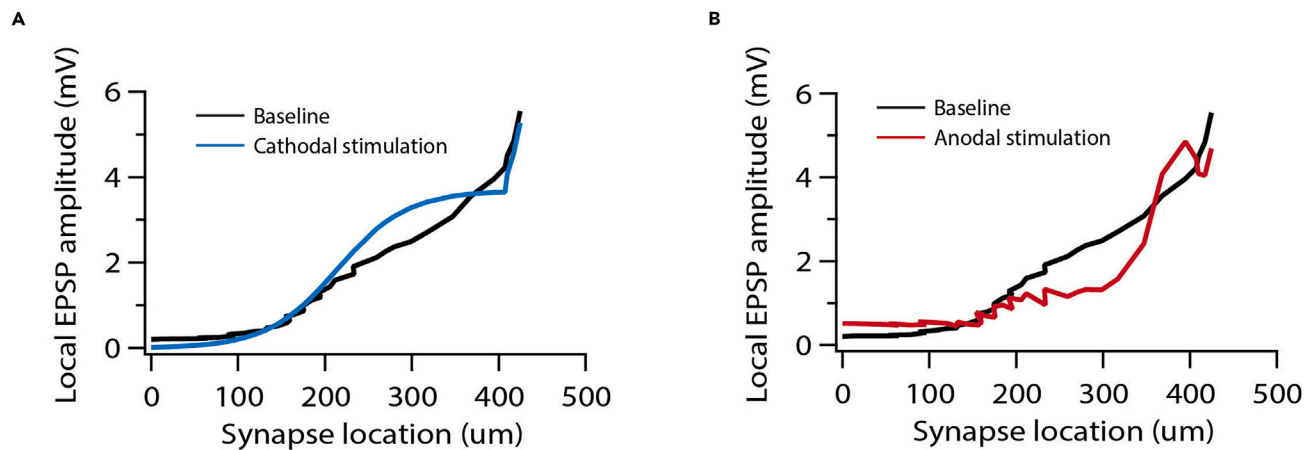
Figure 3. tDCS modifies the local EPSP amplitude along the dendrite
(A) Cathodal stimulation increases local EPSP amplitude toward the distal dendritic region.
(B) Anodal stimulation decreases local EPSP amplitude toward the distal dendritic region.

tDCS modulates the backpropagating action potential morphology

Another important aspect of dendritic physiology is backpropagating action potential (bAP), which affects long-term synaptic plasticity.[16,17] Since bAP properties are affected by membrane potential and the state of various voltage-dependent channels,[18] we used our model to investigate whether tDCS affects bAP amplitude. In doing so, we found that cathodal stimulation increased bAP amplitude in the distal dendrite (Figure 4A), whereas anodal stimulation did not alter bAP amplitude (Figure 4B).

To understand the biophysical mechanism for the observed phenomenon, we looked into the inactivating dynamics of A-type K^+ channels, as previously suggested.[19] For this, we first constructed an inactivation curve of A-type K^+ channels (Figures 4C and 4D). As discussed earlier, under baseline conditions, membrane potential was at −65 mV (black vertical line in Figures 4C and 4D). At this membrane potential, almost 75% of total conductance was available for activation. During cathodal stimulation, membrane potential shifted toward −60 mV (blue vertical line in Figure 4C). This shift in membrane potential caused the inactivation of an additional 15% of the total conductance, such that total conductance available for activation was reduced to ∼60%. This reduction in total conductance available for activation contributes toward an increase in bAP amplitude. On the other hand, during anodal stimulation, membrane potential shifted to −70 mV (red vertical line in Figure 4D), which recovered almost 5% of the total conductance from inactivation, making the total conductance available for activation to increase to ∼80%. However, at the distal dendritic location, bAP amplitude is small and from −70 mV it is not able to activate much additional A-type K^+ conductance, which does not allow much of a change in the bAP amplitude, thus maintaining a similar profile to that of the baseline condition.

Dendritic effects of anodal and cathodal tDCS modulate neuronal input/output relationship

Observing these effects led us to question whether these effects of tDCS lead to modulation of neuronal input/output relationship. To do this, we utilized a model previously published by us.[12,13] We placed in our model only α-amino-3-hydroxy-5-methyl-4-isoxazolepropionic acid (AMPA) receptor-type synapses throughout the main neuronal trunk. A spike generator was used to feed inputs to the synapses at predetermined required frequencies. The input/output relationship of the model neuron was determined by stimulating synapses at various frequencies. For any given input frequency (1–50 Hz in steps of 1 Hz), all synapses were stimulated simultaneously using independent Poisson-distributed input timings, and this was repeated for 20 times for a given stimulus frequency. Each trial ran for 1 s, and the number of action potentials fired was taken as the response frequency. This simulation showed that tDCS affects the input/output relationship significantly (Figures 5A and 5B). Specifically, cathodal stimulation slightly increased the firing rate (Figure 5A), whereas anodal stimulation slightly decreased the firing rate (Figure 5B) ($F_{(49,1862)}$ = 9.55, p < 0.0001 and $F_{(49,1862)}$ = 7.52, p < 0.0001 for interaction of stimulation and frequency in two-way ANOVA for cathodal and anodal, respectively). These effects were observed with the lower to mid stimulus frequencies, with significant Bonferroni-corrected *post hoc* differences (p < 0.05) in 10–31 Hz range for cathodal tDCS and in 9–23 Hz range for anodal tDCS.

tDCS modulates synaptic plasticity in distal dendrites

Given our findings of effects of tDCS on EPSP and bAP, and the multiple studies that showed a role of tDCS in modulating synaptic plasticity in general,[20–24] we aimed to explore the impact that tDCS would have on long-term synaptic plasticity from a dendritic standpoint. Using our previously published approach with the herein model,[13] we investigated whether tDCS modifies LTP. Specifically, we placed AMPA-NMDA receptor-type synapse throughout the main neuronal trunk. Permeability values of N-methyl-D-aspartate (NMDA) receptors were defined by NMDA-to-AMPA ratio (NAR) for any given synapse, which was set to be 1.5 for all synapses. To induce synaptic plasticity, individual synapses were assigned a stimulus frequency by random sampling from the uniform distribution in the range of 4–12 Hz. All synapses were stimulated
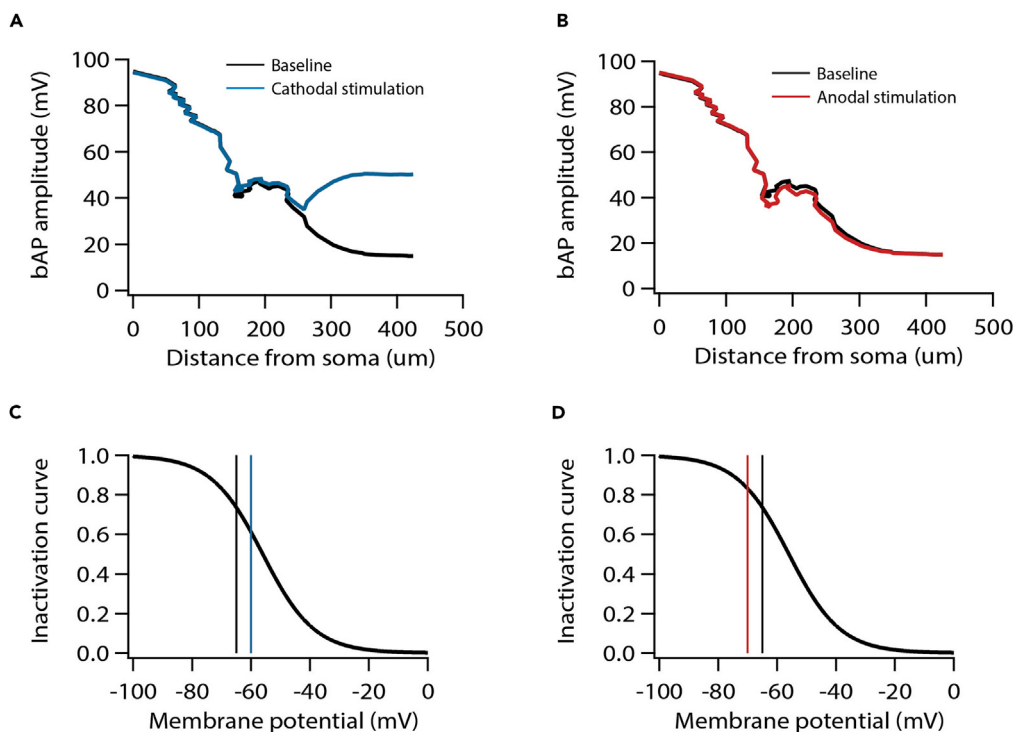
Figure 4. Cathodal and anodal tDCS differentially modifies the backpropagating action potential amplitude at the distal region of the dendrite

(A) Cathodal stimulation increases backpropagating action potential amplitude at the distal region of the dendrite.

(B) Anodal stimulation does not affect backpropagating action potential amplitude at distal dendrite.

(C) Steady-state inactivation curve of A-type K$^+$ channels showing availability of channels for opening at rest (black vertical line) and during cathodal stimulation (blue vertical line).

(D) Steady-state inactivation curve of A-type K$^+$ channels showing availability of channels for opening at rest (black vertical line) and during anodal stimulation (red vertical line).

simultaneously, and stimulating timings of synapses were determined by independent Poisson distributions. Owing to synaptic stimulation, and the consequent entry of Ca^{++} from NMDA receptors and T-type Ca^{++} channels, synaptic weights evolved based on intracellular Ca^{++} levels. At the end of the simulation, given that starting synaptic weight was determined at 0.25, most synapses expressed LTP, whereas few synapses underwent long-term depression (LTD) (Figures 6A and 6B). Following this, we introduced our tDCS model to examine its effects on synaptic plasticity, by computing the synaptic weights under various tDCS conditions and plotting these synaptic weights against the synaptic weights obtained under the baseline condition (Figures 6A and 6B). As evident from the graphs (Figures 6A and 6B), during cathodal stimulation the magnitude of LTP was increased in a subset of synapses ($t_{(81)} = 3.09$, $p < 0.01$ in paired t-test between baseline and cathodal tDCS) (Figure 6A), whereas during anodal stimulation the magnitude of LTP was decreased in a subset of synapses ($t_{(81)} = 2.03$, $p < 0.05$ in paired t-test between baseline and anodal tDCS) (Figure 6B).

At this stage, we did not know the location of these synapses along the dendritic trunk. Specifically, we did not know whether these synapses are distributed throughout the dendritic trunk or are they confined within a small stretch of the dendritic trunk. Our previous analyses on input resistance (Figure 2), local EPSP amplitude (Figure 3), and bAP amplitude (Figure 4) showed that the modulatory effect of tDCS was confined to the distal portion of the dendritic trunk where tDCS' effect was maximal. Hence, we predicted that these synapses will also be confined to the distal portion of the dendritic trunk. In order to test this, we plotted the synaptic weight values under the different tDCS conditions and the baseline condition, against the location of the synapses along the dendritic trunk (Figures 6C and 6D). As predicted, the effect of tDCS on synaptic plasticity was largely confined to the synapses at the most distal portion of the dendritic trunk (>350 μm from the soma) ($t_{(11)} = 6.21$, $p < 0.0001$ and $t_{(11)} = 3.54$, $p < 0.01$ in paired t test between baseline and cathodal and baseline and anodal, respectively] (Figures 6C and 6D).

DISCUSSION

tDCS has been shown to be beneficial for various clinical indications,[1] but its mechanistic basis at the cellular level has not been fully understood. To this end, in this study, using a morphologically and biophysically realistic conductance-based neuronal model, we show that tDCS has a significant role in modulating dendritic input resistance (Figure 2), local EPSP amplitude (Figure 3), bAP amplitude (Figure 4), input/output relationship (Figure 5), and synaptic plasticity (Figure 6). All these effects of tDCS were mostly confined to the distal end of the dendrite,
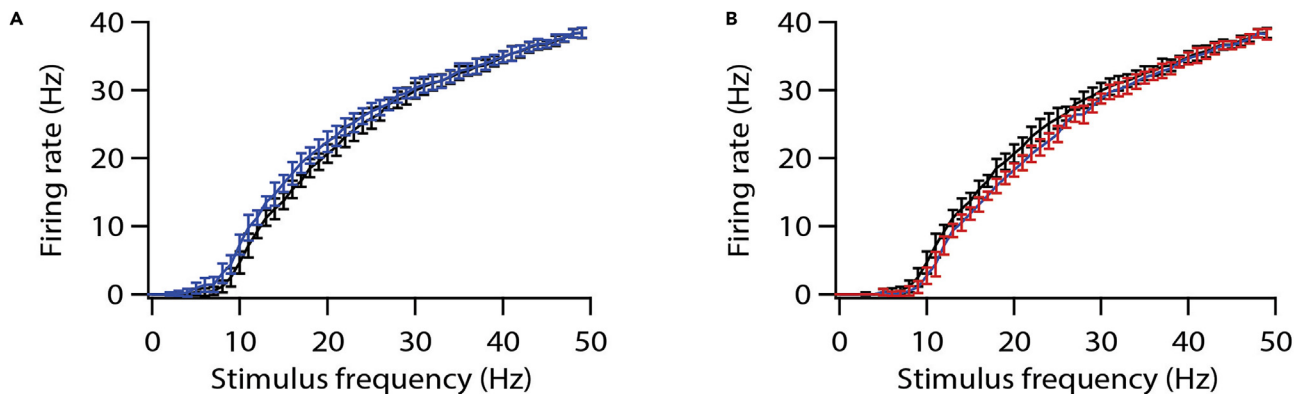
Figure 5. The dendritic effects of tDCS are sufficient to induce a small but significant change in cellular excitability as observed by shifting the low to middle range of the input-output relationship curve in our model

(A) Input-output curve under baseline (no stimulation) condition (black) and during cathodal stimulation (blue). Cathodal stimulation enhances excitability shown in left shift of the input-output relationship curve in the low to medium stimulation range. ($F_{(49,1862)}$ = 9.55, p < 0.0001; two-way ANOVA for interaction of stimulus frequency and firing rate between cathodal and baseline conditions).

(B) Input-output curve under baseline (no stimulation) condition (black) and during anodal stimulation (red). Anodal stimulation reduces excitability shown in the right shift of the input-output relationship curve in the low to medium stimulation range. ($F_{(49,1862)}$ = 7.52, p < 0.0001; two-way ANOVA for interaction of stimulus frequency and firing rate between anodal and baseline conditions)]. Data are presented as Mean ± SD.

where tDCS-induced polarization of the dendrite is more robust (Figure 1). Although tDCS had significant effects on dendritic input resistance (Figure 2), local EPSP amplitude (Figure 3), bAP amplitude (Figure 4), input/output relationship (Figure 5), and synaptic plasticity (Figure 6), we observed that tDCS' effects on neuronal input/output relationship in our model system were quite weak compared to other measurements and were evident only in the low to mid range of stimulation frequencies. These intriguing and conflicting results call for reconciliation, and there could be several reasons for this.

One of the reasons for this discrepancy could be simulation run time. We ran our simulations for only 1 s. It is quite possible that if we run the simulations for longer timescales, such as those that relate to behavioral timescales, the difference between the input/output relationship under baseline and tDCS conditions might get enhanced and encompass even lower and especially higher stimulation frequencies. The other reason could be the number of synapses. Cathodal/anodal stimulations affect only the small distal portion of the dendrite. In that small portion of the dendrite, we introduced only a few synapses (less than 10) in our model system. The small number of synapses in the distal portion of the dendrite could account for the weak effect of tDCS on the input/output relationship. Moreover, to simplify our model to some extent, synapses were present only on the apical dendritic trunk and not on the oblique dendrites. If synapses were present on oblique dendrites, they also could have contributed to a stronger difference between the input/output relationships under baseline and tDCS conditions.

Our findings are also interesting given the microanatomical structures of neural circuits and the cellular position of synaptic connections between neurons. Since we observed that tDCS affects mainly the synapses at the most distal portion of the dendrite, it is expected that it will either enhance or diminish these distal synaptic inputs depending upon whether it is cathodal or anodal stimulation, respectively. Such synaptic inputs are present superficially in the cortex in layer-1, at the location of the dendritic tufts of layer-2/3 and layer-5 pyramidal cells. This is particularly important since this superficial layer is the closest to the stimulation electrodes, where the current density of tDCS is the strongest. Nonetheless, these distal dendritic inputs are also present in deeper brain structures where there is a flow of tDCS current such as the dorsal hippocampus where entorhinal cortex layer-2/3 neurons make synaptic connections in the stratum lacunosum-moleculare. Therefore, it stands to reason that tDCS will affect dendritic spike generation in such distal dendritic regions as well, thereby affecting synaptic plasticity at these synapses.[25,26] Furthermore, as cathodal stimulation enhances bAP amplitude, it will also affect synaptic plasticity in the distal region of the dendrites through co-incident detection of synaptic inputs and bAP, in coincidence with the model of spike timing-dependent plasticity (STDP).[16,17,27] On the other hand, anodal stimulation will probably not induce opposite effects, given its minimal effects on bAP amplitude (Figure 4B).

The issue of asymmetry concerning tDCS effects on bAP, where cathodal stimulation that depolarizes the dendrite enhanced bAP amplitude, while anodal stimulation that hyperpolarizes the distal dendrite hardly affected bAP amplitude, aligns with other previous observations regarding tDCS' non-linearity. Although these asymmetrical effects of tDCS were raised long ago in several studies,[4,28] the cellular origin of this asymmetry is not entirely understood. We previously reported similar asymmetry of DCS effects on axonal physiology, where depolarization of axon using anodal stimulation entailed a stronger effect compared with cathodal stimulation.[29,30] Nonetheless, these two asymmetric effects are generated by different mechanisms, where in dendrites the asymmetry probably stems from the effects on A-type K^+ channels inactivation by depolarization (Figures 4C and 4D), and in the axon it is generated by differences in inactivation/activation of sodium and calcium channels.[29,30]
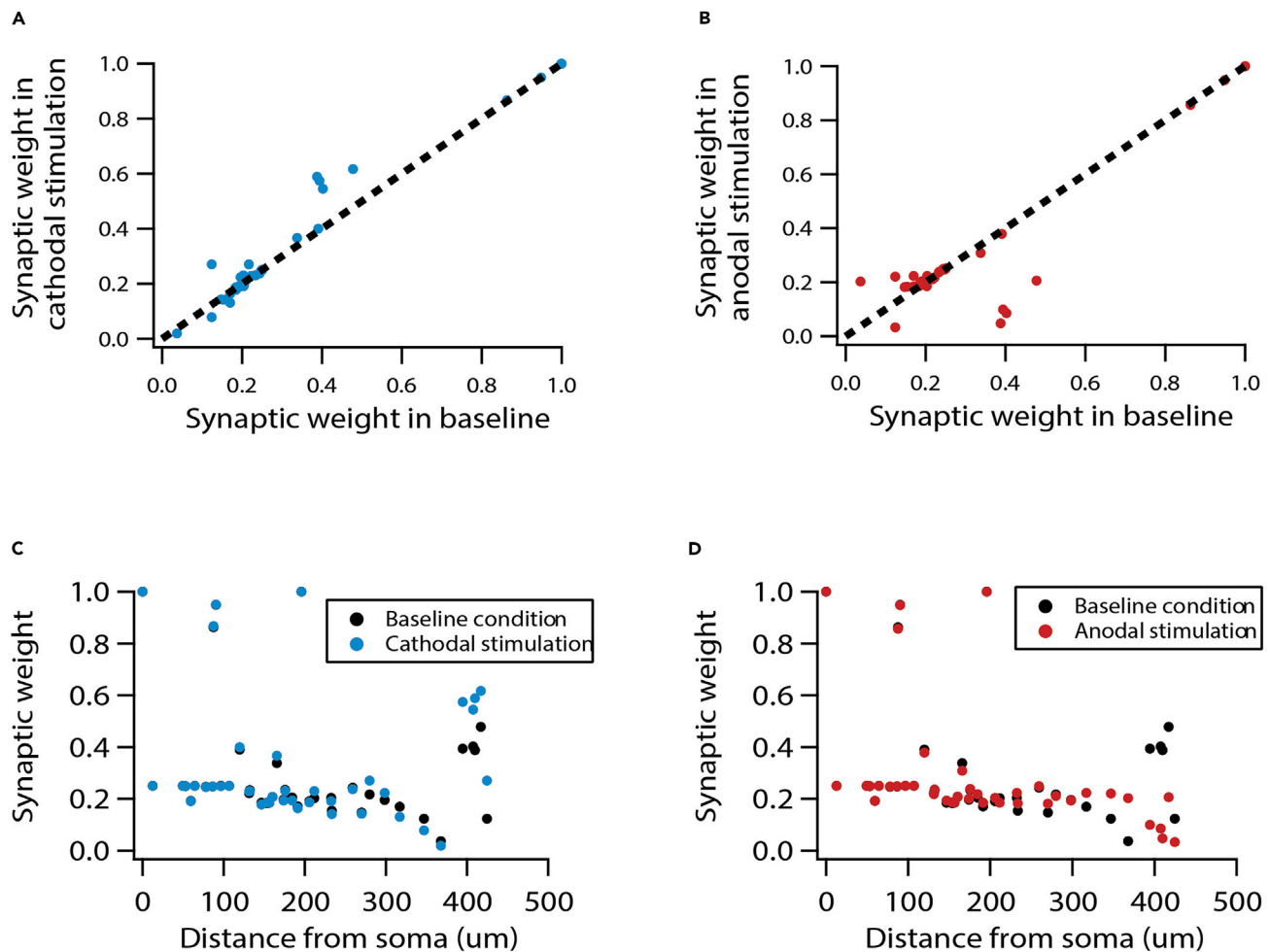
Figure 6. tDCS modulates synaptic plasticity

(A) Cathodal stimulation enhances LTP at distal dendritic synapses.

(B) Anodal stimulation reduces LTP at distal dendritic synapses.

(C) Distribution of synaptic weights with respect to location of the synapse under baseline condition and during cathodal stimulation shows that the largest increase of synaptic weights is in the distal dendritic region. The LTP-induced changes in synaptic weights is statistically significant ($t_{(11)} = 6.21$, $p < 0.0001$ in paired t test).

(D) Distribution of synaptic weights with respect to location of the synapse under baseline condition and during anodal stimulation shows that the largest decrease of synaptic weights is in the distal dendritic region. The LTP-induced changes in synaptic weights were statistically significant ($t_{(11)} = 3.54$, $p < 0.01$; in paired t test).

The results of our model show that tDCS' effects are mostly limited to the distal portion where membrane polarization is sufficient to modulate differential ionic conductance. Noteworthily, in our model this region was relatively short, given our estimation of a dendritic length constant ranging from 211 μm for cathodal tDCS to a dendritic length constant of 232 μm for anodal tDCS. These simulations of differential length constants yielded a decay of polarization along the dendrite from its maximal value at the dendritic tip. However, in real life, the distal affected portion can be much longer, in particular the region of dendritic tufts, as the length constants of these thin elongated structures are probably much longer. Thus, a significant membrane polarization should take a more substantial region of the dendrite, affecting many more synapses subsequently inducing stronger synaptic plasticity effects.

Another limitation of the attempt to simulate a real brain condition is the contribution of glial cells to the dendritic physiology, especially astrocytes. There is evidence to support that astrocytes are also target cells for tDCS.[31,32] Since astrocytes are important structure in the tripartite synapses,[33] the effects of tDCS might contribute to the modulation of spontaneous excitatory postsynaptic currents (sEPSCs). Nonetheless, the star-shaped astrocytes are relatively symmetric, which probably reduce their sensitivity to electrical field application. Yet, their elongated processes that are aligned with the electrical field vector are expected to be polarized, although, due to differential effects of cathodal versus anodal stimulation, this polarization might not be completely symmetric. And indeed, studies showed that prolonged application of tDCS modulated the calcium dynamics in astrocytes, which could subsequently alter neuronal activity and synaptic plasticity.[34,35]

tDCS has been shown to induce after-effects at various fronts.[4,36,37] Usually, aftereffects were seen in prolonged stimulations (minutes) and not in brief ones (seconds). Moreover, the aftereffects are considered to involve synaptic plasticity.[38] Within the framework of the herein study, we speculate that tDCS could induce aftereffects related to various physiologically relevant measurements. Specifically, during cathodal stimulation membrane potential will get depolarized, which will induce calcium entry into the neurons through voltage-gated calcium channels. Prolonged stimulation in the order of multiple minutes will generate an accumulation of intracellular calcium leading to protracted enhanced calcium levels, which have the potential to trigger various signaling cascades. These calcium-dependent signaling cascades could subsequently lead to changes in neuronal physiology through modulation of various voltage-gated ion channels and postsynaptic receptors. These aftereffects could be related to neuronal excitability, firing rate, or backpropagating action potential. These measurements have been shown to undergo changes with various activity protocols.[15,39–45]

In conclusion, we show that tDCS exerts modulatory influence on dendritic physiology and that this effect is mostly confined to the distal region of the neuronal dendritic trunk. Moreover, our results show that these dendritic effects have potential implications for the long-term effects of tDCS and the manner by which tDCS exerts its clinical effects.

Limitations of the study

The study has several limitations. Due to the need for a detailed morphologically realistic, 3D reconstructed neuron, we utilized a model of a hippocampal CA1 pyramidal neuron that we had plenty of experience from previous studies.[12,13] However, tDCS' strongest electrical field is applied at the cortex, affecting mostly cortical pyramidal neurons. Despite multiple similarities between cortical pyramidal neurons and hippocampal CA1 pyramidal neurons, the two types of neurons also contain several differences. Furthermore, we did not consider in our model the opposite polarization at the distal portion of the axon that tDCS generates. This opposite polarization at the axon terminal might induce additional excitability and plasticity effects that were not considered. In addition, despite using a realistic model, to keep the simulations feasible, the model has to be kept simplified to some extent. These limitations are elaborated in details in the text.

STAR★METHODS

Detailed methods are provided in the online version of this paper and include the following:

- KEY RESOURCES TABLE
- RESOURCE AVAILABILITY
  - Lead contact
  - Materials availability
  - Data and code availability
- EXPERIMENTAL MODEL AND STUDY PARTICIPANT DETAILS
- METHODS DETAILS
  - General computational and simulation details
  - Passive membrane properties
  - Voltage-gated ion channels kinetics and distribution
  - Synapse model
  - Synaptic weight update mechanism
  - Measurements
- QUANTIFICATION AND STATISTICAL ANALYSIS

AUTHOR CONTRIBUTIONS

H.K. Conceptualization; H.K. Funding Acquisition; H.K. and R.K.R. Methodology; R.K.R. Investigation; R.K.R. and H.K. Formal Analysis; R.K.R. and H.K. Visualization; H.K. supervision; R.K.R and H.K. Writing Original Draft; R.K.R and H.K. Writing – Review and Editing

DECLARATION OF INTERESTS

The authors declare no competing interests.

REFERENCES

1. Lefaucheur, J.-P., Antal, A., Ayache, S.S., Benninger, D.H., Brunelin, J., Cogiamanian, F., Cotelli, M., De Ridder, D., Ferrucci, R., Langguth, B., et al. (2017). Evidence-based guidelines on the therapeutic use of transcranial direct current stimulation (tDCS). Clin. Neurophysiol. *128*, 56–92. https://doi.org/10.1016/j.clinph.2016.10.087.

2. Nitsche, M.A., Liebetanz, D., Tergau, F., and Paulus, W. (2002). Modulation of cortical excitability by transcranial direct current stimulation. Nervenarzt *73*, 332–335.

3. Priori, A., Berardelli, A., Rona, S., Accornero, N., and Manfredi, M. (1998). Polarization of the human motor cortex through the scalp. Neuroreport *9*, 2257–2260.

4. Nitsche, M.A., Fricke, K., Henschke, U., Schlitterlau, A., Liebetanz, D., Lang, N., Henning, S., Tergau, F., and Paulus, W. (2003). Pharmacological modulation of cortical excitability shifts induced by transcranial direct current stimulation in humans. J. Physiol. *553*, 293–301. https://doi.org/10.1113/jphysiol.2003.049916.

5. Tranchina, D., and Nicholson, C. (1986). A model for the polarization of neurons by extrinsically applied electric fields. Biophys. J. *50*, 1139–1156. https://doi.org/10.1016/S0006-3495(86)83558-5.

6. Chan, C.Y., Hounsgaard, J., and Nicholson, C. (1988). Effects of electric fields on transmembrane potential and excitability of turtle cerebellar Purkinje cells in vitro. J. Physiol. *402*, 751–771.

7. Bikson, M., Inoue, M., Akiyama, H., Deans, J.K., Fox, J.E., Miyakawa, H., and Jefferys, J.G.R. (2004). Effects of uniform extracellular DC electric fields on excitability in rat hippocampal slices in vitro. J. Physiol. *557*, 175–190. https://doi.org/10.1113/jphysiol.2003.055772.

8. Matsunaga, K., Nitsche, M.A., Tsuji, S., and Rothwell, J.C. (2004). Effect of transcranial DC sensorimotor cortex stimulation on somatosensory evoked potentials in humans. Clin. Neurophysiol. *115*, 456–460. https://doi.org/10.1016/s1388-2457(03)00362-6.

9. Kunori, N., and Takashima, I. (2019). Evaluation of acute anodal direct current stimulation-induced effects on somatosensory-evoked responses in the rat. Brain Res. *1720*, 146318. https://doi.org/10.1016/j.brainres.2019.146318.

10. Datta, A., Krause, M.R., Pilly, P.K., Choe, J., Zanos, T.P., Thomas, C., and Pack, C.C. (2016). On comparing in vivo intracranial recordings in non-human primates to predictions of optimized transcranial electrical stimulation. Annu. Int. Conf. IEEE Eng. Med. Biol. Soc. *2016*, 1774–1777. https://doi.org/10.1109/EMBC.2016.7591061.

11. Rathour, R.K., and Narayanan, R. (2014). Homeostasis of functional maps in active dendrites emerges in the absence of individual channelostasis. Proc. Natl. Acad. Sci. USA *111*, E1787–E1796. https://doi.org/10.1073/pnas.1316599111.

12. Rathour, R.K., and Kaphzan, H. (2022). Voltage-Gated Ion Channels and the Variability in Information Transfer. Front. Cell. Neurosci. *16*, 906313. https://doi.org/10.3389/fncel.2022.906313.

13. Rathour, R.K., and Kaphzan, H. (2023). Synergies between synaptic and HCN channel plasticity dictates firing rate homeostasis and mutual information transfer in hippocampal model neuron. Front. Cell.

14. Rathour, R.K., Malik, R., and Narayanan, R. (2016). Transient potassium channels augment dendritic degeneracy in hippocampal active dendritic spectral tuning. Sci. Rep. *6*, 24678. https://doi.org/10.1038/srep24678.

15. Narayanan, R., and Johnston, D. (2007). Long-term potentiation in rat hippocampal neurons is accompanied by spatially widespread changes in intrinsic oscillatory dynamics and excitability. Neuron *56*, 1061–1075. https://doi.org/10.1016/j.neuron.2007.10.033.

16. Spruston, N. (2008). Pyramidal neurons: dendritic structure and synaptic integration. Nat. Rev. Neurosci. *9*, 206–221. https://doi.org/10.1038/nrn2286.

17. Stuart, G., Spruston, N., Sakmann, B., and Häusser, M. (1997). Action potential initiation and backpropagation in neurons of the mammalian CNS. Trends Neurosci. *20*, 125–131. https://doi.org/10.1016/s0166-2236(96)10075-8.

18. Brunner, J., and Szabadics, J. (2016). Analogue modulation of back-propagating action potentials enables dendritic hybrid signalling. Nat. Commun. *7*, 13033. https://doi.org/10.1038/ncomms13033.

19. Migliore, M., Hoffman, D.A., Magee, J.C., and Johnston, D. (1999). Role of an A-type K+ conductance in the back-propagation of action potentials in the dendrites of hippocampal pyramidal neurons. J. Comput. Neurosci. *7*, 5–15.

20. Kronberg, G., Bridi, M., Abel, T., Bikson, M., and Parra, L.C. (2017). Direct Current Stimulation Modulates LTP and LTD: Activity Dependence and Dendritic Effects. Brain Stimul. *10*, 51–58. https://doi.org/10.1016/j.brs.2016.10.001.

21. Agboada, D., Mosayebi-Samani, M., Kuo, M.-F., and Nitsche, M.A. (2020). Induction of long-term potentiation-like plasticity in the primary motor cortex with repeated anodal transcranial direct current stimulation – Better effects with intensified protocols? Brain Stimul. *13*, 987–997. https://doi.org/10.1016/j.brs.2020.04.009.

22. Watanabe, Y., Dezawa, S., Takei, H., Nagasaka, K., and Takashima, I. (2023). Hippocampal-prefrontal long-term potentiation-like plasticity with transcranial direct current stimulation in rats. Neurobiol. Learn. Mem. *201*, 107750. https://doi.org/10.1016/j.nlm.2023.107750.

23. Farahani, F., Kronberg, G., FallahRad, M., Oviedo, H.V., and Parra, L.C. (2021). Effects of direct current stimulation on synaptic plasticity in a single neuron. Brain Stimul. *14*, 588–597. https://doi.org/10.1016/j.brs.2021.03.001.

24. Frase, L., Mertens, L., Krahl, A., Bhatia, K., Feige, B., Heinrich, S.P., Vestring, S., Nissen, C., Domschke, K., Bach, M., and Normann, C. (2021). Transcranial direct current stimulation induces long-term potentiation-like plasticity in the human visual cortex. Transl. Psychiatry *11*, 17. https://doi.org/10.1038/s41398-020-01134-4.

25. Golding, N.L., Staff, N.P., and Spruston, N. (2002). Dendritic spikes as a mechanism for cooperative long-term potentiation. Nature *418*, 326–331. https://doi.org/10.1038/nature00854.

26. Kim, Y., Hsu, C.-L., Cembrowski, M.S., Mensh, B.D., and Spruston, N. (2015). Dendritic

sodium spikes are required for long-term potentiation at distal synapses on hippocampal pyramidal neurons. Elife *4*, e06414. https://doi.org/10.7554/eLife.06414.

27. Waters, J., Schaefer, A., and Sakmann, B. (2005). Backpropagating action potentials in neurones: Measurement, mechanisms and potential functions. Prog. Biophys. Mol. Biol. *87*, 145–170. https://doi.org/10.1016/j.pbiomolbio.2004.06.009.

28. Lafon, B., Rahman, A., Bikson, M., and Parra, L.C. (2017). Direct Current Stimulation Alters Neuronal Input/Output Function. Brain Stimul. *10*, 36–45. https://doi.org/10.1016/j.brs.2016.08.014.

29. Vasu, S.O., and Kaphzan, H. (2021). The role of sodium channels in direct current stimulation—axonal perspective. Cell Rep. *37*, 109832.

30. Vasu, S.O., and Kaphzan, H. (2022). Calcium channels control tDCS-induced spontaneous vesicle release from axon terminals. Brain Stimul. *15*, 270–282. https://doi.org/10.1016/J.BRS.2022.01.005.

31. Mishima, T., Nagai, T., Yahagi, K., Akther, S., Oe, Y., Monai, H., Kohsaka, S., and Hirase, H. (2019). Transcranial Direct Current Stimulation (tDCS) Induces Adrenergic Receptor-Dependent Microglial Morphological Changes in Mice. eneuro *6*. ENEURO.0204-0219. https://doi.org/10.1523/ENEURO.0204-19.2019.

32. Monai, H., Ohkura, M., Tanaka, M., Oe, Y., Konno, A., Hirai, H., Mikoshiba, K., Itohara, S., Nakai, J., Iwai, Y., and Hirase, H. (2016). Calcium imaging reveals glial involvement in transcranial direct current stimulation-induced plasticity in mouse brain. Nat. Commun. *7*, 11100. https://doi.org/10.1038/ncomms11100.

33. Perea, G., Navarrete, M., and Araque, A. (2009). Tripartite synapses: astrocytes process and control synaptic information. Trends Neurosci. *32*, 421–431. https://doi.org/10.1016/j.tins.2009.05.001.

34. Monai, H., and Hirase, H. (2018). Astrocytes as a target of transcranial direct current stimulation (tDCS) to treat depression. Neurosci. Res. *126*, 15–21. https://doi.org/10.1016/j.neures.2017.08.012.

35. Callai, E.M.M., Zin, L.E.F., Catarina, L.S., Ponzoni, D., Gonçalves, C.A.S., Vizuete, A.F.K., Cougo, M.C., Boff, J., Puricelli, E., Fernandes, E.K., et al. (2022). Evaluation of the immediate effects of a single transcranial direct current stimulation session on astrocyte activation, inflammatory response, and pain threshold in naïve rats. Behav. Brain Res. *428*, 113880. https://doi.org/10.1016/j.bbr.2022.113880.

36. Nitsche, M.A., and Paulus, W. (2000). Excitability changes induced in the human motor cortex by weak transcranial direct current stimulation. J. Physiol. *527*, 633–639. https://doi.org/10.1111/j.1469-7793.2000.t01-1-00633.x.

37. Nitsche, M.A., Doemkes, S., Karaköse, T., Antal, A., Liebetanz, D., Lang, N., Tergau, F., and Paulus, W. (2007). Shaping the effects of transcranial direct current stimulation of the human motor cortex. J. Neurophysiol. *97*, 3109–3117. https://doi.org/10.1152/jn.01312.2006.

38. Bikson, M., Paulus, W., Esmaeilpour, Z., Kronberg, G., and Nitsche, M.A. (2019). In Mechanisms of Acute and After Effects of Transcranial Direct Current Stimulation

BT - Practical Guide to Transcranial Direct Current Stimulation: Principles, Procedures and Applications, H. Knotkova, M.A. Nitsche, M. Bikson, and A.J. Woods, eds. (Springer International Publishing), pp. 81–113. https://doi.org/10.1007/978-3-319-95948-1_3.

39. Fan, Y., Fricker, D., Brager, D.H., Chen, X., Lu, H.C., Chitwood, R.A., and Johnston, D. (2005). Activity-dependent decrease of excitability in rat hippocampal neurons through increases in I(h). Nat. Neurosci. *8*, 1542–1551. https://doi.org/10.1038/nn1568.

40. Narayanan, R., Dougherty, K.J., and Johnston, D. (2010). Calcium store depletion induces persistent perisomatic increases in the functional density of h channels in hippocampal pyramidal neurons. Neuron *68*, 921–935. https://doi.org/10.1016/j.neuron.2010.11.033.

41. Campanac, E., Daoudal, G., Ankri, N., and Debanne, D. (2008). Downregulation of dendritic I(h) in CA1 pyramidal neurons after LTP. J. Neurosci. *28*, 8635–8643. https://doi.org/10.1523/JNEUROSCI.1411-08.2008.

42. Brager, D.H., and Johnston, D. (2007). Plasticity of intrinsic excitability during long-term depression is mediated through mGluR-dependent changes in I(h) in hippocampal CA1 pyramidal neurons. J. Neurosci. *27*, 13926–13937.

43. Lin, M.T., Luján, R., Watanabe, M., Adelman, J.P., and Maylie, J. (2008). SK2 channel plasticity contributes to LTP at Schaffer collateral-CA1 synapses. Nat. Neurosci. *11*, 170–177.

44. Frick, A., Magee, J., and Johnston, D. (2004). LTP is accompanied by an enhanced local excitability of pyramidal neuron dendrites. Nat. Neurosci. *7*, 126–135. https://doi.org/10.1038/nn1178.

45. Kim, J., Jung, S.C., Clemens, A.M., Petralia, R.S., and Hoffman, D.A. (2007). Regulation of dendritic excitability by activity-dependent trafficking of the A-type K+ channel subunit Kv4.2 in hippocampal neurons. Neuron *54*, 933–947.

46. Carnevale, N.T., and Hines, M.L. (2006). The NEURON Book (Cambridge University Press).

47. Ascoli, G.A., Donohue, D.E., and Halavi, M. (2007). NeuroMorpho.Org: a central resource for neuronal morphologies. J. Neurosci. *27*, 9247–9251. https://doi.org/10.1523/JNEUROSCI.2055-07.

48. Johnston, D., and Wu, S.M.S. (1995). Foundations of Cellular Neurophysiology (The MIT Press).

49. Hoffman, D.A., Magee, J.C., Colbert, C.M., and Johnston, D. (1997). K+ channel regulation of signal propagation in dendrites of hippocampal pyramidal neurons. Nature *387*, 869–875.

50. Magee, J.C. (1998). Dendritic hyperpolarization-activated currents modify the integrative properties of hippocampal CA1 pyramidal neurons. J. Neurosci. *18*, 7613–7624.

51. Narayanan, R., and Johnston, D. (2008). The h channel mediates location dependence and plasticity of intrinsic phase response in rat hippocampal neurons. J. Neurosci. *28*, 5846–5860.

52. Poolos, N.P., Migliore, M., and Johnston, D. (2002). Pharmacological upregulation of h-channels reduces the excitability of pyramidal neuron dendrites. Nat. Neurosci. *5*, 767–774. https://doi.org/10.1038/nn891nn891.

53. Shah, M.M., Migliore, M., Valencia, I., Cooper, E.C., and Brown, D.A. (2008). Functional significance of axonal Kv7 channels in hippocampal pyramidal neurons. Proc. Natl. Acad. Sci. USA *105*, 7869–7874. https://doi.org/10.1073/pnas.0802805105.

54. Magee, J.C., and Johnston, D. (1995). Characterization of single voltage-gated Na+ and Ca2+ channels in apical dendrites of rat CA1 pyramidal neurons. J. Physiol. *487*, 67–90.

55. Fleidervish, I.A., Lasser-Ross, N., Gutnick, M.J., and Ross, W.N. (2010). Na+ imaging reveals little difference in action potential-evoked Na+ influx between axon and soma. Nat. Neurosci. *13*, 852–860. https://doi.org/10.1038/nn.2574.

56. Narayanan, R., and Johnston, D. (2010). The h current is a candidate mechanism for regulating the sliding modification threshold in a BCM-like synaptic learning rule. J. Neurophysiol. *104*, 1020–1033. https://doi.org/10.1152/jn.01129.2009.

57. Honnuraiah, S., and Narayanan, R. (2013). A calcium-dependent plasticity rule for HCN channels maintains activity homeostasis and stable synaptic learning. PLoS One *8*, e55590. https://doi.org/10.1371/journal.pone.0055590PONE-D-12-31521.

58. Mayer, M.L., and Westbrook, G.L. (1987). Permeation and block of N-methyl-D-aspartic acid receptor channels by divalent cations in mouse cultured central neurones. J. Physiol. *394*, 501–527.

59. Canavier, C.C. (1999). Sodium dynamics underlying burst firing and putative mechanisms for the regulation of the firing pattern in midbrain dopamine neurons: a computational approach. J. Comput. Neurosci. *6*, 49–69.

60. Jahr, C.E., and Stevens, C.F. (1990). Voltage dependence of NMDA-activated macroscopic conductances predicted by single-channel kinetics. J. Neurosci. *10*, 3178–3182.

61. Jahr, C.E., and Stevens, C.F. (1990). A quantitative description of NMDA receptor-channel kinetic behavior. J. Neurosci. *10*, 1830–1837.

62. Poirazi, P., Brannon, T., and Mel, B.W. (2003). Arithmetic of subthreshold synaptic summation in a model CA1 pyramidal cell. Neuron *37*, 977–987.

63. Dingledine, R., Borges, K., Bowie, D., and Traynelis, S.F. (1999). The glutamate receptor ion channels. Pharmacol. Rev. *51*, 7–61.

64. Shouval, H.Z., Bear, M.F., and Cooper, L.N. (2002). A unified model of NMDA receptor-dependent bidirectional synaptic plasticity. Proc. Natl. Acad. Sci. USA *99*, 10831–10836. https://doi.org/10.1073/pnas.152343099.

65. Magee, J.C., and Cook, E.P. (2000). Somatic EPSP amplitude is independent of synapse location in hippocampal pyramidal neurons. Nat. Neurosci. *3*, 895–903. https://doi.org/10.1038/78800.

STAR★METHODS

KEY RESOURCES TABLE

REAGENT or RESOURCE	SOURCE	IDENTIFIER
Software and algorithms		
NEURON simulation environment	Carnevale & Hines. *The NEURON Book.*[46]	Neuron.yale.edu/neuron/
IGOR Pro	WaveMetrics, Inc.	www.wavemetrics.com
Prism	GraphPad Software, Inc.	www.graphpad.com

RESOURCE AVAILABILITY

Lead contact

Further information and requests for resources and reagents should be directed to and will be fulfilled by the Lead Contact, Hanoch Kaphzan (hkaphzan@univ.haifa.ac.il).

Materials availability

This study did not generate new unique reagents.

Data and code availability

- This study did not generate new datasets.
- All computational and simulation details are within this paper, and a ZIP file containing the simulations codes that were used in this study is in supplemental material.
- Any additional information required to reanalyze the data reported in this work paper is available from the lead contact upon request.

EXPERIMENTAL MODEL AND STUDY PARTICIPANT DETAILS

This section does not apply to our study, as no participants were recruited.

METHODS DETAILS

General computational and simulation details

A morphologically realistic, 3D reconstructed, hippocampal CA1 pyramidal neuron (*n123*), obtained from Neuromorpho.org[47] was used as the substrate for all simulations. Morphology and modeling parameters of passive membrane properties and voltage-gated ion channels (VGICs) were the same as those used in previous studies[12,13] which were originally developed in[11] and are detailed below.

We employed NEURON simulation environment (v8.0)[46] for all simulations. For all simulations, the temperature was set at 34°C, and ion-channels kinetics was appropriately adjusted based upon experimentally determined q10 factors. The integration time constant, for solving various differential equations, was set to be 25 μs. In absence of tDCS, membrane potential was fixed at −65 mV and simulations were run at this potential. Data analyses were done using custom-built software written within IGOR Pro (v8.0) (Wavematrics).

Given that tDCS induces membrane potential polarization, we roughly modeled the tDCS condition by directly injecting a constant current into the distal region of the dendrite. Injected current amplitude was ±200 pA depending on whether it is cathodal or anodal stimulation. This type of current injection yielded approximately ±5 mV deflection in membrane potential in the most distal portion of the dendrite.

We estimated dendritic length constant by injecting a constant current at distal portion of the dendrite. The distance required along the apical trunk for 63.2% decay of voltage response was taken as length constant.[48]

Passive membrane properties

Passive membrane parameters were set such that the model neuron was able to capture experimental statistics of various measurements.[15,19,49–51] Explicitly, specific membrane capacitance (C_m) was set at 1 μF/cm² across the entire morphology. Specific membrane resistivity (R_m) and intracellular resistivity (R_a) were distributed non-uniformly and varied along the somato-apical trunk as functions of the radial distance of the compartment from the soma (x) using the following formulation:

$$R_m(x) = R_m - \max + \frac{(R_m - \min - R_m - \max)}{1 + \exp((R_m - d - x)/R_m - k)}$$

(Equation 1)

$$R_a(x) = R_a - \max + \frac{(R_a - \min - R_a - \max)}{1 + \exp((R_a - d - x)/R_a - k)} \qquad \text{(Equation 2)}$$

where R_m-max = 125 kΩ/cm^2 and R_a-max = 120 Ω/cm were default values at the soma, and R_m-min = 85 kΩ/cm^2 and R_a-min = 70 Ω/cm were values assigned to the terminal end of the apical trunk (which was ~425 μm distance from the soma for the reconstruction under consideration). The other default values were: R_m-d = R_a-d = 300 μm, R_m-k = R_a-k = 50 μm; R_a-k = 14 μm. The basal dendrites and the axonal compartments had somatic R_m and R_a. Model neuron with these distributions of passive membrane properties was compartmentalized using d_λ rule[46] to ensure that each compartment was smaller than $0.1\lambda_{100}$, where λ_{100} was the space constant computed at 100 Hz. This produced a total of 809 compartments in the model neuron.

Voltage-gated ion channels kinetics and distribution

The model neuron used expressed five conductance-based voltage-gated ion channels (VGICs): Na$^+$, A-type K$^+$ (KA), delayed rectifier K$^+$ (KDR), T-type Ca^{++} (CaT), and hyperpolarization-activated h (HCN) channels. Na$^+$, KDR, and KA channels were modeled based upon previous kinetic schemes,[19] and h channels were modeled as in.[52] T-type Ca^{++} channels kinetics was taken from.[53] Na$^+$, K$^+$, and h channels models were based upon Hodgkin-Huxley formalism and had reversal potentials 55, –90, and −30 mV respectively. The CaT current was modeled using the Goldman-Hodgkin-Katz (GHK) formulation with the default values of external and internal Ca^{++} concentrations set at 2 mM and 100 nM, respectively. The Densities of Na and KDR conductances were kept uniform across the neuronal arbor, whereas the densities of h, CaT, and KA channel conductances increased on the apical side with an increase in distance from the soma.[49,50,54] The basal dendritic compartments had somatic conductance values.

Uniformly distributed Na and KDR conductances were set at 16 and 10 mS/cm^2, respectively. Na conductance was 5-fold higher in the axon initial segment compared to the somatic counterpart[55] and the rest of the axon was treated as passive. To account for the slow inactivation of dendritic Na$^+$ channels, an additional inactivation gating variable was included for dendritic Na$^+$ channels.[19] KA conductance was set as a linearly increasing gradient as a function of radial distance from the soma, x,[49] using the following formulation:

$$\overline{g}_{KA}(x) = A - g_B (1 + A - Fx/100) \qquad \text{(Equation 3)}$$

where somatic $\overline{g}_{KA}$ was 3.1 mS/cm^2, and A-F (=8) quantified the slope of this linear gradient. In order to incorporate experimental observations related to differences in half-maximal activation voltage ($V_{1/2}$) between the proximal and the distal KA channels in CA1 pyramidal cells,[49] two distinct models of KA channels were adopted. A proximal model was used for compartments with radial distances less than 100 μm from the soma, and beyond that point a distal A-type K$^+$ conductance model was used.

The increase in maximal h conductance along the somato-apical axis as a function of radial distance from the soma, x, was modeled using the following formulation:

$$\overline{g}_h(x) = h - g_B \left(1 + \frac{h - F}{1 + \exp((h - d - x)/h - k)}\right) \qquad \text{(Equation 4)}$$

where h-g_b denotes maximal h conductance at the soma, set to be 25 μS/cm^2, and h-F (=12) formed fold increase along the somato-apical axis. Half-maximal distance of $\overline{g}_h$ increase, h-d was 320 μm, and the parameter quantifying the slope, h-k was 50 μm. To accommodate the experimental observations regarding changes in $V_{1/2}$ of the activation of h conductance at various locations along the somato-apical trunk,[50] the half-maximal activation voltage for h channels was −82 mV for $x \leq 100$ μm, linearly varied from −82 mV to −90 mV for 100μm $\leq x \leq 300$ μm, and −90 mV for $x > 300$ μm.

The CaT conductance gradient was modeled as a sigmoidal increase with increasing radial distance from the soma, x:

$$\overline{g}_{CaT}(x) = T - g_B \left(1 + \frac{T - F}{1 + \exp((T - d - x)/T - k)}\right) \qquad \text{(Equation 5)}$$

where T-g_B denotes maximal CaT conductance at the soma, set to be 80 μS/cm^2, and T-F (=30) formed fold increase along the somato-apical axis. Half-maximal distance of $\overline{g}_{CaT}$ increase, T-d was 350 μm, and the parameter quantifying the slope, T-k was 50 μm. These parametric constraints accounted for the experimental constraints on the coexistence of the six functional maps along the same somato-apical trunk.[11]

Synapse model

A synapse was modeled as a co-localization of AMPA and NMDA receptor currents as described previously.[56,57] A spike generator was used to feed inputs to the synapses at predetermined required frequencies. The default value of the NMDA:AMPA permeability ratio was set at 1.5. Both receptors currents were modeled based upon GHK formulation. The current through NMDA receptors was set as the combination of Na$^+$, K$^+$, and Ca^{++}, and their voltage and time dependence were described by the following equations:

$$I_{NMDA}(v, t) = I_{NMDA}^{Na}(v, t) + I_{NMDA}^{K}(v, t) + I_{NMDA}^{Ca}(v, t) \qquad \text{(Equation 6)}$$

where

$$I_{NMDA}^{Na}(v,t) = \overline{P}_{NMDA} P_{Na} s(t) MgB(v) \frac{vF^2}{RT} \left\{ \frac{[Na]_i - [Na]_o \exp\left(-\frac{vF}{RT}\right)}{1 - \exp\left(-\frac{vF}{RT}\right)} \right\} \qquad \text{(Equation 7)}$$

$$I_{NMDA}^{K}(v,t) = \overline{P}_{NMDA} P_{K} s(t) MgB(v) \frac{vF^2}{RT} \left\{ \frac{[K]_i - [K]_o \exp\left(-\frac{vF}{RT}\right)}{1 - \exp\left(-\frac{vF}{RT}\right)} \right\} \qquad \text{(Equation 8)}$$

$$I_{NMDA}^{Ca}(v,t) = \overline{P}_{NMDA} P_{Ca} s(t) MgB(v) \frac{4vF^2}{RT} \left\{ \frac{[Ca]_i - [Ca]_o \exp\left(-\frac{2vF}{RT}\right)}{1 - \exp\left(-\frac{2vF}{RT}\right)} \right\} \qquad \text{(Equation 9)}$$

where F is Faraday's constant, R is the gas constant and T is the temperature in Kelvin. $\overline{P}_{NMDA}$ is the maximum permeability of the NMDA receptor and the default ratio of values of P_{Ca}, P_{Na}, and P_K was set to be 10.6:1:1, respectively, owing to experimental observations.[58,59] The external and internal concentrations of the various ions were set as follows (in mM): $[Na]_o = 140$, $[Na]_i = 18$, $[K]_o = 5$, $[K]_i = 140$, $[Ca]_o = 2$, $[Ca]_i = 100 \times 10^{-6}$. This resulted in equilibrium potentials for sodium and potassium ions of +55 and −90 mV, respectively. $MgB(v)$ and $s(t)$ denote magnesium dependence and temporal evolution of NMDA current, respectively, and were defined as follows[60,61]:

$$MgB(v) = \left\{ 1 + \frac{[Mg]_o \exp(-0.062v)}{3.57} \right\}^{-1} \qquad \text{(Equation 10)}$$

where $[Mg]_o$ denotes extracellular magnesium concentration and was set to 2 mM.

$$s(t) = a\left[\exp\left(-\frac{t}{\tau_d}\right) - \exp\left(-\frac{t}{\tau_r}\right)\right] \qquad \text{(Equation 11)}$$

where a is the normalization constant to ensure that $0 \leq s(t) \leq 1$. τ_r and τ_d denote the rise and decay time constants of NMDA receptor-mediated current, respectively, and were set to be 5 and 50 ms, respectively.

The evolution of intracellular calcium, consequent to entry from NMDA receptors and T-type Ca^{++} channels, was modeled as described previously[56,62]:

$$\frac{d[Ca]_i}{dt} = -\frac{10,000\, I_{NMDA}^{Ca}}{3.6 \cdot dpt \cdot F} + \frac{[Ca]_\infty - [Ca]_i}{\tau_{Ca}} \qquad \text{(Equation 12)}$$

where $\tau_{Ca} = 30$ ms is the calcium decay time constant, $dpt = 0.1$ μm is the depth of the shell and $[Ca]_\infty = 10^{-4}$ mM is the steady-state value of $[Ca]_i$.

The current through AMPA receptors was mediated by the combination of Na$^+$ and K$^+$ currents and was defined as follows:

$$I_{AMPA}(v,t) = I_{AMPA}^{Na}(v,t) + I_{AMPA}^{K}(v,t) \qquad \text{(Equation 13)}$$

where

$$I_{AMPA}^{Na}(v,t) = \overline{P}_{AMPA}\, w P_{Na} s(t) \frac{vF^2}{RT} \left\{ \frac{[Na]_i - [Na]_o \exp\left(-\frac{vF}{RT}\right)}{1 - \exp\left(-\frac{vF}{RT}\right)} \right\} \qquad \text{(Equation 14)}$$

$$I_{AMPA}^{K}(v,t) = \overline{P}_{AMPA}\, w P_{K} s(t) \frac{vF^2}{RT} \left\{ \frac{[K]_i - [K]_o \exp\left(-\frac{vF}{RT}\right)}{1 - \exp\left(-\frac{vF}{RT}\right)} \right\} \qquad \text{(Equation 15)}$$

where $\overline{P}_{AMPA}$ is the maximum permeability of AMPA receptors. The default ratio of P_{Na} and P_K values was set to be 1:1 owing to experimental observations.[63] $s(t)$ denotes the temporal evolution of AMPA current and was modeled as in Equation 11 with τ_r and τ_d set to be 2 and 10 ms, respectively. w is the weight parameter that undergoes activity-dependent update (See section synaptic weight update mechanism). To generate presynaptic spike, we used NEURON simulation environment's built-in network connection object, Netcon.

Synaptic weight update mechanism

A synaptic weight parameter, w, associated with the specific synapse of the given compartment was updated based upon the intracellular calcium concentration of the given compartment. This dependence of synaptic weight parameter, w, on intracellular calcium concentration was defined by the following equation based upon the calcium control hypothesis[64]:

$$\frac{dw}{dt} = \eta([Ca]_i)\left[\Omega([Ca]_i) - w\right] \tag{Equation 16}$$

where $\eta([Ca]_i)$ is the calcium-dependent learning rate and was dependent upon learning time constant $\tau([Ca]_i)$ as follows:

$$\eta([Ca]_i) = \frac{1}{\tau([Ca]_i)} \tag{Equation 17}$$

where $\tau([Ca]_i)$ was defined as:

$$\tau([Ca]_i) = P_1 + \frac{P_2}{P_3 + [Ca]_i^{P_4}} \tag{Equation 18}$$

with $P_1 = 1$ s, $P_2 = 0.1$ s, $P_3 = P_2 \times 10^{-4}$ and $P_4 = 3$. The values of these parameters warrant that when $[Ca] \approx 0$, $\tau([Ca]_i) \approx 3$ h.

$\Omega([Ca]_i)$ has the following form:

$$\Omega([Ca]_i) = 0.25 + \frac{1}{1+\exp\left\{-\beta_2\left([Ca]_i - \alpha_2\right)\right\}} - 0.25\frac{1}{1+\exp\left\{-\beta_1\left([Ca]_i - \alpha_1\right)\right\}} \tag{Equation 19}$$

with $\alpha_1 = 0.35$, $\alpha_2 = 0.55$, $\beta_1 = 80$ and $\beta_2 = 80$. The default initial value of w, w_{init}, was set at 0.25.

Measurements

The input/output relationship of the model neuron was determined by stimulating synapses at various frequencies. For any given input frequency, all synapses were stimulated simultaneously using independent Poisson distributed input timings and this was repeated for 20 times for every given stimulus frequency. Each trial ran for 1 s and the number of action potentials fired was taken as the response frequency.

EPSP amplitude was computed by activating a given synapse at a given location, and the corresponding potential was recorded. The difference between baseline potential and peak EPSP response was taken as EPSP amplitude. For computing synaptically driven input/output response profile and EPSP amplitude, only AMPA receptor type conductance was used.[65]

The input resistance of the model neuron at various locations along the neuronal trunk was computed by injecting a current pulse of various amplitudes (−50 to +50 in steps of 10 pA) and the corresponding local steady-state voltage response was recorded to compute V–I relationship. The slope of the linear fit to the V–I curve was determined as the input resistance.

QUANTIFICATION AND STATISTICAL ANALYSIS

All simulations were performed using NEURON programming environment.[46] All data analyses and plotting were done using custom-written scripts within IGOR Pro (Wavemetrics). Statistical analyses of 2-way ANOVA and paired t-test were performed where necessary in Prism (GraphPad Software).